eprints@whiterose.ac.uk
https://eprints.whiterose.ac.uk/

An isogeometric continuum shell element for non-linear analysis

Saman Hosseini[a], Joris J. C. Remmers[a], Clemens V. Verhoosel[a], René de Borst[b,*]

[a]*Eindhoven University of Technology, Department of Mechanical Engineering, PO BOX 513, 5600 MB, Eindhoven, The Netherlands.*
[b]*University of Glasgow, School of Engineering, Rankine Building, Oakfield Avenue, Glasgow G12 8LT, UK.*

Abstract

An isogeometric continuum shell formulation is proposed in which NURBS basis functions are used to construct the reference surface of the shell. Through-the-thickness behavior is interpolated using a higher-order B-spline which is in contrast to the standard continuum shell (solid-like shell) formulation where a linear Lagrange shape function is typically used in the thickness direction. The present formulation yields a complete isogeometric representation of the continuum shell. The shell element is implemented in a standard finite element code using Bézier extraction which facilitates numerical integration on the reference surface of the shell. Through-the-thickness integration is done using a connectivity array which determines the support of a B-spline basis function over an element. The formulation has been verified using different linear and geometrically non-linear examples. The ability of the formulation in modelling buckling of static delaminations in composite materials is also demonstrated.

Keywords: Isogeometric analysis, continuum shell element, solid-like shell element, Bézier extraction, delamination

1. Introduction

Isogeometric analysis (IGA) has recently received much attention in the computational mechanics community. The basic idea is to use splines, which are the functions commonly used in computer-aided design (CAD) to describe the geometry, as the basis function for the analysis rather than the traditional Lagrange basis functions [1, 2]. Originally, Non-Uniform Rational B-Splines (NURBS) have been used in isogeometric analysis, but their inability to achieve local refinement has driven their gradual replacement by T-splines [3].

A main advantage of isogeometric analysis is that the functions used for the representation of the geometry are employed directly for the analysis, thereby by-passing the need for a sometimes elaborate meshing procedure. This important feature allows for a design-through-analysis procedure which yields a significant reduction of the time needed for the preparation of the analysis model [2]. Indeed, the exact parametrization of the geometry can have benefits for the numerical simulation of shell structures, which can be very sensitive to imperfections in the geometry. Moreover, the higher-order continuity of the shape functions used in isogeometric analysis allows for a straightforward implementation of shell theories which require C^1 continuity such as Kirchhoff-Love models [4, 5]. A Reissner-Mindlin shell formulation has been developed by Benson *et al.* [6] using NURBS basis functions. Although C^1 continuity is then no requisite, good results and a high degree of robustness were reported for large deformation problems. In addition, the exact geometry description allows for an exact computation of the shell director [7]. Recently, the 7-parameter shell model [8] was cast in an isogeometric formulation in Ref. [9].

A further benefit of basis functions that possess a higher degree of continuity is that the computation of stresses is vastly improved. In shell analysis this can be particularly important when materially non-linear phenomena such as damage, or delamination, which can occur in laminated structures, are included in the analysis. In the latter case the computation of an accurate three-dimensional stress field becomes mandatory, and solid-like shell elements become an obvious choice [10, 11]. This shell element is characterized by the absence of rotational degrees of freedom, which is convenient when stacking them, yet possesses shell kinematics, and is rather insensitive to shear locking and membrane locking,

A partially isogeometric solid-like shell element was developed in Ref. [12]. This element combines the advantage of an accurate geometric description of the shell mid-surface with the three-dimensional stress representation of conventional solid-like shell elements. The formulation adopts NURBS (or T-spline) basis functions for the discretization of the shell mid-surface, while in the thickness direction conventional Lagrange polynomials have been used. As a next step, in this contribution we adopt a higher-order interpolation in the thickness direction, which makes use of B-spline basis functions. An important advantage of using B-spline basis functions is their ability to model weak and strong discontinuity in the displacement field by knot insertion [13]. This is less straightforward using conventional finite elements. Weak discontinuities are usually introduced by subdividing the shell in the thickness direction in multiple layers with each a piecewise polynomial interpolation, e.g. References [14, 15]. Strong discontinuities (delaminations) can be modelled using interface elements, or in a more general manner, by exploiting the partition-of-unity property of

---

*Corresponding author: René de Borst, University of Glasgow, School of Engineering, Rankine Building, Oakfield Avenue, Glasgow G12 8LT, UK.
Email address: `Rene.DeBorst@glasgow.ac.uk` (René de Borst)

Lagrange polynomials [16].

The continuum shell formulation is outlined in Section 2. In Section 3 we review the basic concepts of isogeometric analysis. Algorithmic and implementation aspects are discussed in Section 4. Section 5 contains a number of examples which assess the performance of the isogeometric continuum shell formulation. The numerical simulations demonstrate the ability of the formulation to model the mechanical behavior of composite structures, including buckling of delaminated panels.

2. Continuum shell formulation

In the solid-like shell element proposed by Parisch [10], an internal stretch term is added to obtain a quadratic term in the displacement field in the thickness direction. As a consequence, the normal strain varies linearly, which significantly reduces membrane locking. The element has been extended in [11, 16] for use in laminated composites, including interlaminar delamination. In Ref. [12] we have described an isogeometric solid-like shell element (SLSBEZ) which utilizes NURBS or T-spline basis functions to construct the mid-surface of the shell. Through the thickness behavior was captured by standard linear shape functions as it is in the conventional solid-like shell element. A complete isogeometric continuum shell element (CSIGA) which is equipped with the B-spline basis functions in the thickness direction is presented here.

2.1. Kinematics

Figure 1 shows the undeformed and the deformed configurations of a continuum shell element. The reference surface of the shell is denoted by S^0. The variables ξ and η are the local curvilinear coordinates in the two independent in-plane directions, and ζ is the local curvilinear coordinate in the thickness direction. The position of a material point within the shell body in the undeformed configuration is written as a function of the three curvilinear coordinates:

$$\mathbf{X}(\xi, \eta, \zeta) = \mathbf{X}^0(\xi, \eta) + \zeta \mathbf{D}(\xi, \eta) \ , \ 0 \le \zeta \le 1 \quad (1)$$

where $\mathbf{X}^0(\xi, \eta)$ is the projection of the point on the reference surface of the shell and $\mathbf{D}(\xi, \eta)$ is the thickness director perpendicular to the surface S_0 at this point.

In any material point, a local reference triad can be established. The covariant base vectors are then obtained as the partial derivatives of the position vectors with respect to the curvilinear coordinates $\Theta^i = [\xi, \eta, \zeta]$. First, we define a set of basis vectors on the reference surface in the undeformed configuration as:

$$\mathbf{E}_\alpha = \frac{\partial \mathbf{X}^0}{\partial \Theta^\alpha} \ , \ \alpha = 1, 2 \quad (2)$$

so that the shell director can be written as:

$$\mathbf{E}_3 = \mathbf{D} = \frac{\mathbf{E}_1 \times \mathbf{E}_2}{\|\mathbf{E}_1 \times \mathbf{E}_2\|} t \quad (3)$$
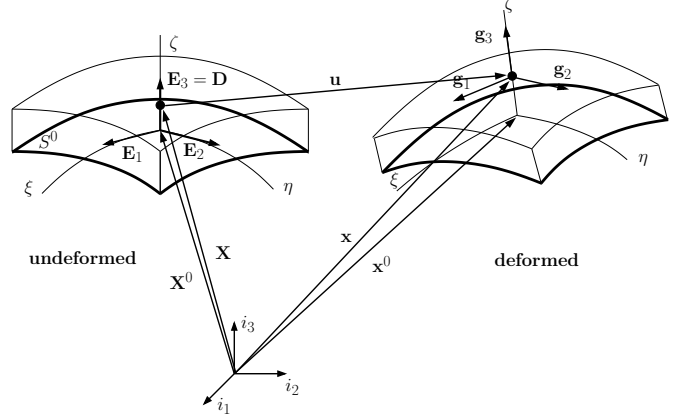
Figure 1: Geometry and kinematics of the shell in the undeformed and in the deformed configurations.

where t is the thickness of the shell. Now, using equation (1), the covariant triad for any point within the shell body is obtained as:

$$\mathbf{G}_\alpha = \frac{\partial \mathbf{X}}{\partial \Theta^\alpha} = \mathbf{E}_\alpha + \zeta \mathbf{D}_{,\alpha} \ , \ \alpha = 1, 2$$

$$\mathbf{G}_3 = \mathbf{D} \quad (4)$$

where the subscript comma denotes partial differentiation.

The position of the material point in the deformed configuration $\mathbf{x}(\xi, \eta, \zeta)$ is related to $\mathbf{X}(\xi, \eta, \zeta)$ via the displacement field $\mathbf{u}(\xi, \eta, \zeta)$ as:

$$\mathbf{x}(\xi, \eta, \zeta) = \mathbf{X}(\xi, \eta, \zeta) + \mathbf{u}(\xi, \eta, \zeta) \quad (5)$$

The displacement field $\mathbf{u}$ can be of any order which is in contrast to the standard solid-like shell formulation where an internal stretch term is added to obtain a quadratic term in the displacement field in the thickness direction. Similarly, in the deformed configuration we can establish the covariant triad as:

$$\mathbf{g}_i = \frac{\partial \mathbf{x}}{\partial \Theta^i} = \mathbf{G}_i + \mathbf{u}_{,i} \ , \ i = 1, 2, 3 \quad (6)$$

which convention will be used in the remainder. Using equations (4) and (6) the metric tensors $\mathbf{G}$ and $\mathbf{g}$ can be determined as:

$$G_{ij} = \mathbf{G}_i \cdot \mathbf{G}_j \ , \ g_{ij} = \mathbf{g}_i \cdot \mathbf{g}_j \ , \ i, j = 1, 2, 3 \quad (7)$$

The contravariant basis vectors needed for the calculation of the strains can be derived as:

$$\mathbf{G}^i = (\mathbf{G})^{-1} \mathbf{G}_i \quad (8)$$

where $(\mathbf{G})^{-1}$ is the inverse of the metric tensor with components G_{ij}. The volume of the element in the undeformed configuration is evaluated using the covariant metric tensor $\mathbf{G}$ in the following manner:

$$d\Omega_0 = \sqrt{\det(\mathbf{G})} \, d\xi \, d\eta \, d\zeta \quad (9)$$

2

2.2. Strain measure

The Green-Lagrange strain tensor $\boldsymbol{\gamma}$ is defined conventionally in terms of deformation gradient $\mathbf{F}$:

$$\boldsymbol{\gamma} = \frac{1}{2}(\mathbf{F}^T \cdot \mathbf{F} - \mathbf{I}) \tag{10}$$

where $\mathbf{I}$ is the unit tensor. The deformation gradient can be written in terms of the base vectors as:

$$\mathbf{F} = \mathbf{g}_i \otimes \mathbf{G}^i \tag{11}$$

which leads to following representation of the Green-Lagrange strain tensor:

$$\boldsymbol{\gamma} = \gamma_{ij}\mathbf{G}^i \otimes \mathbf{G}^j \quad \text{with} \quad \gamma_{ij} = \frac{1}{2}(g_{ij} - G_{ij}) \tag{12}$$

where the summation convention has been used for repeated indices. Substituting equations (4) and (6) for G_{ij} and g_{ij} into this relation yields:

$$\gamma_{ij} = \frac{1}{2}(\mathbf{G}_i \cdot \mathbf{u}_{,j} + \mathbf{u}_{,i} \cdot \mathbf{G}_j + \mathbf{u}_{,i} \cdot \mathbf{u}_{,j}) \tag{13}$$

2.3. Material law

In continuum shell elements the stresses are computed using a three-dimensional constitutive relation. Assuming small strains, a linear relation between the rates of the Second Piola-Kirchhoff stress tensor $\mathbf{S}$ and the Green-Lagrange strain tensor can be adopted:

$$\mathcal{D}\mathbf{S} = \mathbb{C} : \mathcal{D}\boldsymbol{\gamma} \tag{14}$$

where $\mathbb{C}$ is the material tangential stiffness matrix.

The strain field in equation (13) is defined in the parametric frame of $\mathbf{G}^i$, $i = 1, 2, 3$, which are not necessarily orthonormal. In order to obtain the strains in the element local frame of reference $\mathbf{T}^i$, they must be transformed using:

$$\gamma_{ij}^L = \gamma_{kl}t_{ki}t_{lj} \ , \ t_{ki} = \mathbf{G}^k \cdot \mathbf{T}^i \tag{15}$$

For an orthotropic material, $\mathbf{T}^1$ is the fiber direction. $\mathbf{T}^2$ and $\mathbf{T}^3$ are the in-plane and out-of-plane normal directions, respectively.

2.4. Virtual work and linearization

In a Total Lagrangian formulation the internal virtual work is expressed in the reference configuration Ω_0:

$$\delta W_{\text{int}} = \int_{\Omega_0} \delta\boldsymbol{\gamma}^T : \mathbf{S} \, d\Omega_0 \tag{16}$$

The resulting system of non-linear equations is typically solved in an incremental-iterative manner, which requires computation of the tangential stiffness matrix. This quantity is obtained by linearizing the internal virtual work, equation (16):

$$\mathcal{D}(\delta W_{int}) = \int_{\Omega_0} (\delta\boldsymbol{\gamma}^T : \mathcal{D}\mathbf{S} + \mathcal{D}(\delta\boldsymbol{\gamma}^T) : \mathbf{S})d\Omega_0 \tag{17}$$

with $\delta\boldsymbol{\gamma}$ and $\mathcal{D}(\delta\boldsymbol{\gamma})$ defined as:

$$\delta\gamma_{ij} = \frac{1}{2}(\mathbf{g}_i \cdot \delta\mathbf{u}_{,j} + \delta\mathbf{u}_{,i} \cdot \mathbf{g}_j) \tag{18}$$

and

$$\mathcal{D}(\delta\gamma_{ij}) = \frac{1}{2}(\mathcal{D}(\mathbf{u}_{,i}) \cdot \delta\mathbf{u}_{,j} + \delta\mathbf{u}_{,i} \cdot \mathcal{D}(\mathbf{u}_{,j})) \tag{19}$$

In an incremental iterative solution scheme, the strain increment $\Delta\boldsymbol{\gamma}$ with respect to the previous converged solution is normally needed. Using equations (13) and (6), it can be derived as:

$$\begin{aligned} \Delta\gamma_{ij} &= \gamma_{ij}(\mathbf{u} + \Delta\mathbf{u}) - \gamma_{ij}(\mathbf{u}) \\ &= \frac{1}{2}(\mathbf{g}_i \cdot \Delta\mathbf{u}_{,j} + \Delta\mathbf{u}_{,i} \cdot \mathbf{g}_j + \Delta\mathbf{u}_{,i} \cdot \Delta\mathbf{u}_{,j}) \end{aligned} \tag{20}$$

3. Isogeometric finite element discretization

In this section we review some basic concepts of isogeometric analysis. Next, the Bézier extraction technique will be outlined. This technique is utilized to make a finite element data structure for the spline basis functions.

3.1. Fundamentals of NURBS and B-splines

A B-spline is a piecewise polynomial curve composed of a linear combination of B-spline basis functions:

$$C(\xi) = \sum_{i=1}^{n} N_{i,p}(\xi)P_i \tag{21}$$

where p is the order and n is the number of the basis functions. The $N_{i,p}(\xi)$ represents a B-spline basis function and the coefficients P_i are points in space, referred to as control points. B-splines are defined over a knot vector, $\boldsymbol{\Xi}$, which is a set of non-decreasing real numbers representing coordinates in the parameter domain:

$$\boldsymbol{\Xi} = [\xi_1, \xi_2, ..., \xi_{n+p+1}] \tag{22}$$

Parametric coordinates ξ_i divide the B-spline into sections. The positive interval $[\xi_1, \xi_{n+p+1}]$ is called an element. If all knots are equally spaced, the knot vector is called uniform, or if they are unequally spaced, they are non-uniform. Between two distinct knots (knot span), a B-spline basis function has C^∞ continuity while it reduces to C^{p-1} across a knot. If a knot value appears k times, the knot is called a multiple knot. At this knot the continuity is C^{p-k}. A B-spline is said to be open if its first and last knots appear $p + 1$ times.

In one dimension, B-spline basis functions are defined using the Cox-de Boor formulation [17, 18] starting with piecewise constants ($p = 0$):

$$N_{i,0}(\xi) = \begin{cases} 1 & \xi_i \le \xi < \xi_{i+1} \\ 0 & \text{otherwise} \end{cases} \tag{23}$$

from which the higher-order functions $p \ge 1$ are derived recursively using:

$$N_{i,p}(\xi) = \frac{\xi - \xi_i}{\xi_{i+p} - \xi_i}N_{i,p-1}(\xi) + \frac{\xi_{i+p+1} - \xi}{\xi_{i+p+1} - \xi_{i+1}}N_{i+1,p-1}(\xi) \tag{24}$$
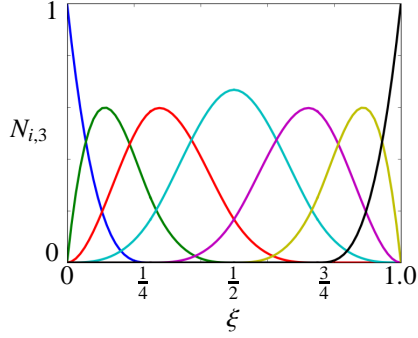
Figure 2: Third-order B-spline basis functions defined over a knot vector $\boldsymbol{\Xi} = [0, 0, 0, 0, \frac{1}{4}, \frac{1}{2}, \frac{3}{4}, 1, 1, 1, 1]$.

Figure 2 shows the B-spline basis functions $N_{i,3}$, defined over the knot vector $\boldsymbol{\Xi} = [0, 0, 0, 0, \frac{1}{4}, \frac{1}{2}, \frac{3}{4}, 1, 1, 1, 1]$. Using tensor products, B-spline surfaces can be constructed using two knot vectors $\boldsymbol{\Xi} = \{\xi_1, \xi_2, ..., \xi_{n+p+1}\}$, $\mathcal{H} = \{\eta_1, \eta_2, ..., \eta_{m+q+1}\}$ and a set of $n \times m$ control points $P_{i,j}$ known as the control net. By defining univariate basis function $N_{i,p}$ and $M_{j,p}$ over these two knot vectors, the B-spline surface is then constructed as

$$S(\xi, \eta) = \sum_{i=1}^{n} \sum_{j=1}^{m} N_{i,p}(\xi) M_{j,q}(\eta) P_{i,j} \qquad (25)$$

B-spline basis functions satisfy the partition of unity property. Also each $N_{i,p}$ has a local support which is contained in the interval $[\xi_i, \xi_{i+p+1}]$. Generally, open B-splines are used in numerical analysis, since they are interpolatory at the boundary, which facilitates the application of Dirichlet boundary conditions.

A drawback of B-splines is their inability to represent engineering objects such as conical sections exactly. For this reason, Non-Uniform Rational B-Splines (NURBS), which encapsulate B-splines and can represent such objects exactly, have become the standard in Computer Aided Design (CAD). NURBS are defined by augmenting each control point with a weight $W_i > 0$ as $P_i = (x_i, y_i, z_i, W_i)$. Such a point can be represented with homogeneous coordinates $P_i^w = (W_i x_i, W_i y_i, W_i z_i, W_i)$ in a projective $\mathbb{R}^4$ space. Accordingly, NURBS basis functions are defined as:

$$R_{\alpha,p} = \frac{N_{\alpha,p}(\xi) W_\alpha}{\mathcal{W}(\xi)} \qquad (26)$$

where $\mathcal{W}(\xi) = \sum_{i=1}^{n} N_{i,p}(\xi) W_i$ is the weighting function. Note that there is no summation implied over the repeated index α, and that a B-spline is recovered when all the weights are equal. The NURBS surfaces are constructed by the weighted tensor product of B-spline functions, similar as done for B-spline surfaces, see equation (25).

3.2. Bézier extraction

As noted in the previous section the parametric coordinates ξ_i in a knot vector divide the parameter domain into elements. Similar to the finite element method, these elements, which refer to the knot intervals $\{\xi_i, \xi_{i+1}\}$ with a positive length, allow for piecewise integration using quadrature rules. Basis functions $N_{i,p}$ have a local support over a knot interval $\{\xi_i, \xi_{i+p+1}\}$, which means that each element supports different basis functions, see Figure 3. This is at variance with the finite element method where numerical integration is done on a single parent element. In order to blend isogeometric analysis into existing finite element computer programs, Bézier elements and Bézier extraction operators are used to provide a finite element structure for B-splines, NURBS [19], and T-splines [20].
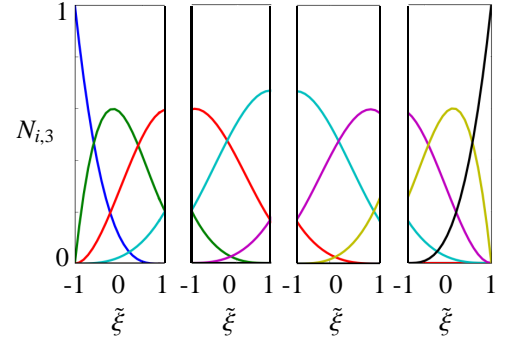
Figure 3: B-spline basis functions plotted over $[-1, 1]$. The basis functions are different per element which is in contrast with standard finite elements.

In general, a degree p Bézier curve is defined by a linear combination of $p + 1$ Bernstein basis functions $\mathbf{B}(\xi)$ [21]. Similar to B-splines, by having an appropriate set of control points, a Bézier curve is written as $C(\xi) = \mathbf{P}^T \mathbf{B}$. A Bézier extraction operator maps a piecewise Bernstein polynomials basis onto a B-spline basis. This transformation makes it possible to use Bézier elements as the finite element representation of B-splines, NURBS, or T-splines.

The extraction operator can be obtained by means of knot insertion. Consider a knot vector $\boldsymbol{\Xi}$ and a set of control points $\{P_k\}_{k=1}^{n}$. By inserting a knot value $\bar{\xi}$ in the knot vector, a new set of control points needs to be calculated. This new set can be related to the initial set of control points via:

$$\bar{\mathbf{P}} = [\mathbf{C}^1]^T \mathbf{P} \qquad (27)$$

This relation ensures that the parametrization is not changed when an existing knot value is repeated, see [19, 21] for algorithms to determine the operator $\mathbf{C}^1$. The knot insertion process is repeated until all interior knots of the knot vector have a multiplicity equal to p, with p the order of the original spline defined over the knot vector $\boldsymbol{\Xi}$. Next, the complete set of new control points $\{\bar{P}_k\}_{k=1}^{m}$, with $m = n_e p + 1$ and n_e the number of elements, is obtained as:

$$\bar{\mathbf{P}} = [\mathbf{C}^{\bar{N}-N}]^T [\mathbf{C}^{\bar{N}-N-1}]^T \cdots [\mathbf{C}^2]^T [\mathbf{C}^1]^T \mathbf{P} = \mathbf{C}^T \mathbf{P} \qquad (28)$$

Again, the parametrization remains unchanged upon the insertion of the additional knots. Hence, according to equation (21) and using equation (28) it is expressed as:

$$C(\xi) = \mathbf{P}^T \mathbf{N}(\xi) = \bar{\mathbf{P}}^T \mathbf{B}(\xi) = (\mathbf{C}^T \mathbf{P})^T \mathbf{B}(\xi) \qquad (29)$$

4

Since **P** is arbitrary, the refined basis functions **B** are related to the original basis functions **N** via:

$$\mathbf{N}(\xi) = \mathbf{CB}(\xi) \tag{30}$$

Hence, every original basis function can be expressed as a linear combination of the Bernstein polynomials. By defining the operators $\mathbf{L}_e$ and $\bar{\mathbf{L}}_e$ to select the basis functions $\mathbf{N}_e$ and $\mathbf{B}_e$ for element e, we have:

$$\mathbf{N}_e = \mathbf{L}_e \mathbf{N} \quad , \quad \mathbf{B} = \bar{\mathbf{L}}_e \mathbf{B}_e \tag{31}$$

Combining equations (30) and (31) leads to

$$\mathbf{N}_e = \mathbf{L}_e \mathbf{C} \bar{\mathbf{L}}_e \mathbf{B}_e \tag{32}$$

The *element* extraction operator $\mathbf{C}_e$ is defined as:

$$\mathbf{N}_e = \mathbf{C}_e \mathbf{B}_e \tag{33}$$

which, using equation (32) can be elaborated as:

$$\mathbf{C}_e = \mathbf{L}_e \mathbf{C} \bar{\mathbf{L}}_e \tag{34}$$

As can be observed from Figure 4, the Bézier extraction operator of an element $\mathbf{C}_e$ maps a piecewise Bernstein polynomial basis onto a B-spline basis.
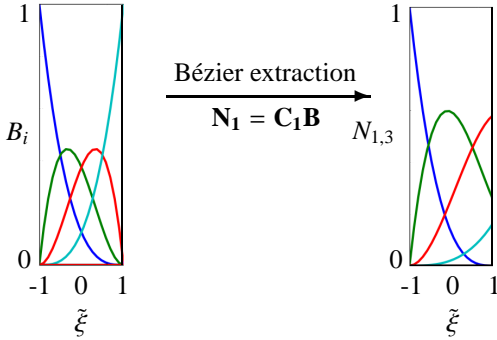
Figure 4: Schematic representation of the Bézier extraction operator.

The Bézier extraction operator for multivatriate B-splines and NURBS can be computed by exploiting their tensor product structure, see [19] for details. For a detailed discussion of Bézier extraction for T-splines, for which a global tensor product structure is absent, see [20]. From the element extraction operator, Bézier elements and the global Bézier mesh can be constructed.

3.3. Isogeometric finite element implementation

Similar to the previous work on the isogeometric solid-like shell element [12], we start by modelling a reference surface S^0 of the shell, where in this case S^0 is the bottom surface of the shell, see Figure 1. Accordingly, the three-dimensional representation of the shell reduces to a bivariate description using Bézier elements, where the geometric and the kinematic quantities are approximated by NURBS functions. Bézier elements for the surface of the shell in combination with linear shape

functions in the thickness direction can fully describe the shell geometry in the undeformed configuration as in equation (1). Therefore, any material point in the shell is obtained as a summation of its projected position vector onto the reference surface, $\mathbf{X}^0$ and its parametric thickness times the shell director, $\zeta \mathbf{D}$.

We assume a higher-order interpolation of the displacement in the thickness direction by using B-spline basis functions. By using equation (24) for example, quadratic B-spline basis functions can be defined over a knot vector $T = [0, 0, 0, \frac{1}{2}, 1, 1, 1]$. Figure 5 shows the resulting basis functions.
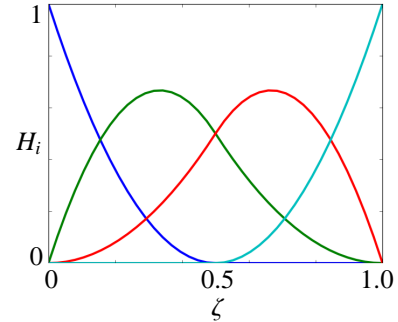
Figure 5: A quadratic B-spline basis function to be used for through the thickness discretization in the deformed configuration. The order of the basis $\{H_i\}_{i=1}^4$ can be chosen arbitrarily.

The total displacement field is now discretized as:

$$\mathbf{u}(\xi, \eta, \zeta) = \sum_{I=1}^{n_{cp}} N_I(\xi, \eta, \zeta) \mathbf{a}_I \tag{35}$$

where $\mathbf{a}_I$ are the displacement degrees of freedom. We assume that n and m are the number of shape functions (or the control points) in the reference surface and in the thickness direction, respectively ($n_{cp} = n \times m$). Hence, the shape functions N_I read:

$$N_I(\xi, \eta, \zeta) = S_i(\xi, \eta) H_j(\zeta),$$

$$I = i + (j - 1)n, \tag{36}$$

$$i \in \{1, ..., n\} \quad , \quad j \in \{1, ..., m\}.$$

where $S_i(\xi, \eta)$ is the basis function from the Bézier element and $H_j(\zeta)$ is the B-spline function in the thickness direction. This equation implies that the trivariate basis functions N_I are decomposed into a surface part and a thickness part which can have different orders of interpolation, p_s and p_h, respectively. As will be detailed below, the strains are subsequently computed from these displacements using shell kinematics.

As we only model a surface of the shell rather than the complete geometry, it is assumed that every control point on the reference surface has $3 \times m$ degrees of freedom, where m is the number of control points in the thickness direction. Therefore, in a Bézier mesh each control point P_i contains a vector of degrees of freedom $\mathbf{\Phi}_i$, as follows:

$$\mathbf{\Phi}_i = [a_x^1, a_y^1, a_z^1, ..., a_x^m, a_y^m, a_z^m]^T \quad , \quad i = 1, 2, ..., n \tag{37}$$

where a_x, a_y, a_z denote the displacement components. Furthermore, by combining equations (35) and (36) the displacement components can be written as follows:

$$u_k(\xi, \eta, \zeta) = \sum_{j=1}^{m} \sum_{i=1}^{n} a_k^{ji} S_i(\xi, \eta) H_j(\zeta) \tag{38}$$

where the subscript k refers to the 1, 2, 3 (or x, y, z) directions.

3.4. Evaluation of internal force vectors and stiffness matrices

For the evaluation of the tangential stiffness matrices we first define the virtual strain vector:

$$\delta\gamma^T = [\delta\gamma_{11}, \delta\gamma_{22}, \delta\gamma_{33}, 2\delta\gamma_{12}, 2\delta\gamma_{23}, 2\delta\gamma_{31}] \tag{39}$$

This vector is related to the control points degrees of freedom as:

$$\delta\gamma = \mathbf{B}\delta\mathbf{\Phi} \tag{40}$$

Referring to equation (18) this equation is expanded as:

$$\delta\gamma = [\mathbf{B}^1\,\mathbf{B}^2\cdots\mathbf{B}^m]_{6\times 3n_{cp}} \cdot [\mathbf{\Phi}^1\,\mathbf{\Phi}^2\cdots\mathbf{\Phi}^m]_{3n_{cp}}^T \tag{41}$$

where

$$[\mathbf{B}^j]_{6\times 3n} \cdot [\mathbf{\Phi}^j]_{3n}^T = [\mathbf{b}^{j1}\,\mathbf{b}^{j2}\cdots b^{jn}] \cdot [\phi^{j1}\,\phi^{j2}\cdots\phi^{jn}]^T \tag{42}$$

In this equation, $\mathbf{b}^{ji}$ a 6×3 matrix with the components:

$$
\begin{aligned}
b_{1k}^{ji} &= \mathbf{g}_1 \cdot \mathbf{i}_k S_{i,\xi} H_j \\[4pt]
b_{2k}^{ji} &= \mathbf{g}_2 \cdot \mathbf{i}_k S_{i,\eta} H_j \\[4pt]
b_{3k}^{ji} &= \mathbf{g}_3 \cdot \mathbf{i}_k S_i H_{j,\zeta} \\[4pt]
b_{4k}^{ji} &= \mathbf{g}_1 \cdot \mathbf{i}_k S_{i,\eta} H_j + \mathbf{g}_2 \cdot \mathbf{i}_k S_{i,\xi} H_j \\[4pt]
b_{5k}^{ji} &= \mathbf{g}_2 \cdot \mathbf{i}_k S_i H_{j,\zeta} + \mathbf{g}_3 \cdot \mathbf{i}_k S_{i,\eta} H_j \\[4pt]
b_{6k}^{ji} &= \mathbf{g}_1 \cdot \mathbf{i}_k S_i H_{j,\zeta} + \mathbf{g}_3 \cdot \mathbf{i}_k S_{i,\xi} H_j
\end{aligned}
\tag{43}
$$

where $\mathbf{i}_k$, $k = 1, 2, 3$ are the unit base vectors of the global coordinate system, and

$$\phi_{ji}^T = [a_x^{ji}\, a_y^{ji}\, a_z^{ji}] \tag{44}$$

with a_k^{ji} used in equation (38). As an example we will derive the explicit expression for the virtual strain component γ_{11} in Appendix A. It is emphasized that the virtual strains and the corresponding $\mathbf{B}$ matrix in equation (40) are stated in the non-orthonormal curvilinear base vectors which should be transformed to the element local frame according to equation (15). The transformed $\mathbf{B}$ matrix is represented by $\mathbf{B}_L$, which is given in Appendix B.

From the internal virtual work, equation (16), the internal force vector is directly obtained as:

$$\mathbf{f}_{\text{int}} = \int_{\Omega_0} \mathbf{B}_L^T \mathbf{S}\, d\Omega_0 \tag{45}$$

Next, we rewrite the linearized internal virtual work, equation (17), in matrix form:

$$
\begin{aligned}
-\mathcal{D}(\delta W_{\text{int}}) &= \delta\mathbf{\Phi}^T \frac{\partial\mathbf{f}_{\text{int}}}{\partial\mathbf{\Phi}} \mathcal{D}\mathbf{\Phi} = \delta\mathbf{\Phi}^T \mathbf{K}\, \mathcal{D}\mathbf{\Phi} \\
&= \delta\mathbf{\Phi}^T (\mathbf{K}^{\text{mat}} + \mathbf{K}^{\text{geom}})\, \mathcal{D}\mathbf{\Phi}
\end{aligned}
\tag{46}
$$

where $\mathbf{K}$ represents the stiffness matrix decomposed in a material part $\mathbf{K}^{\text{mat}}$ and a geometric part, $\mathbf{K}^{\text{geom}}$, as usual. From equation (17) these matrices can be obtained as:

$$\mathbf{K}^{\text{mat}} = \int_{\Omega_0} \mathbf{B}_L^T \mathbf{C}\mathbf{B}_L\, d\Omega_0 \quad,\quad \mathbf{K}^{\text{geom}} = \int_{\Omega_0} \frac{\partial\mathbf{B}_L^T}{\partial\mathbf{\Phi}} \mathbf{S}\, d\Omega_0 \tag{47}$$

The geometric part is the stress-dependent part of the stiffness matrix and is obtained through the derivatives of the virtual strains, equation (19). Using the notation:

$$\omega_{kl} = t_{ki} t_{lj} S_{ij} \tag{48}$$

with S_{ij} the components of the Second Piola-Kirchhoff stress tensor and t_{ki} defined in equation (15), the integrand of the geometrical part of the stiffness matrix can be written as:

$$\frac{\partial\mathbf{B}_L^T}{\partial\mathbf{\Phi}} = \mathbf{\Lambda}^T \mathbf{\Lambda} \tag{49}$$

where

$$\mathbf{\Lambda}^T = [\lambda^1, \lambda^2, \cdots, \lambda^m]_{3n_{cp}\times 3} \tag{50}$$

with

$$\lambda^j = [\lambda^{j1}, \lambda^{j2}, \cdots, \lambda^{jn}]_{3n\times 3}^T \tag{51}$$

and

$$
\begin{aligned}
\lambda^{ji} = [\; &S_{i,\xi} H_j \sqrt{\omega_{11}} + S_{i,\eta} H_j \sqrt{\omega_{22}} + S_i H_{j,\zeta} \sqrt{\omega_{33}} \\
&+ (S_{i,\xi} H_j + S_{i,\eta} H_j) \sqrt{\omega_{12}} \\
&+ (S_{i,\eta} H_j + S_i H_{j,\zeta}) \sqrt{\omega_{23}} \\
&+ (S_{i,\xi} H_j + S_i H_{j,\zeta}) \sqrt{\omega_{13}} \;]\mathbf{I}
\end{aligned}
\tag{52}
$$

Herein, i refers to layer i and $\mathbf{I}$ is the 3×3 unit matrix.

4. Numerical aspects

The linearized internal virtual work relation derived in equation (17) is discretized using B-spline basis functions. A distinction is made between the discretization of the in-plane and the out-of-plane displacement fields. Regarding the latter, we will derive three variants. In the first variant, all layers of the shell element are represented by a single higher-order B-spline in the thickness direction. In the second variant, interfaces between layers are represented by weak discontinuities. In the third version of the element a static delamination is modelled by introducing a strong discontinuity in the B-spline function.

6

4.1. In-surface and out-of-surface integration

As mentioned in the formulation of B-splines and NURBS, the basis functions are defined over a parametric knot span, i.e $(\xi, \eta, \zeta) \in [0, 1]^3$. In order to carry out the numerical integration the basis functions and their derivatives should be calculated locally at quadrature points defined over a parent element, i.e $(\tilde{\xi}, \tilde{\eta}, \tilde{\zeta}) \in [-1, 1]^3$. Moreover the corresponding Jacobian determinant of the mapping must be calculated. The mapping for all the parametric coordinates is the same. For example, for a thickness element of $[\zeta_k, \zeta_{k+1}]$ the mapping is (Figure 6):

$$\zeta = \zeta_k + (\tilde{\zeta} + 1)\frac{\zeta_{k+1} - \zeta_k}{2} \tag{53}$$

where $\tilde{\zeta}$ is the parent element coordinate. Therefore the kinematic parameters in terms of B-spline and NURBS parametric coordinate should be written in the right format. For instance, equation (4) is rewritten as:

$$\mathbf{G}_\alpha = \frac{\partial \mathbf{X}}{\partial \Theta^{\tilde{\alpha}}} = \mathbf{E}_{\tilde{\alpha}} + \left(\zeta_k + (\tilde{\zeta} + 1)\frac{\zeta_{k+1} - \zeta_k}{2}\right)\mathbf{D}_{,\tilde{\alpha}} \quad, \quad \tilde{\alpha} = 1, 2$$

$$\mathbf{G}_3 = \frac{\partial \mathbf{X}}{\partial \tilde{\zeta}} = \frac{\zeta_{k+1} - \zeta_k}{2}\mathbf{D}$$

$$\tag{54}$$

As we employ independent discretizations for the reference surface of the shell and for the thickness direction, the numerical integration schemes in the in-plane and out-of-plane directions will also be decoupled. Accordingly, the Bézier extraction operator will be used for the integration over the surface. First, the geometry of the reference surface is mapped to its corresponding NURBS parametric space $(\xi, \eta) \in [0, 1]^2$, see Figure 7. Then, the second mapping is carried out to the Bézier space where the parent element $(\tilde{\xi}, \tilde{\eta}) \in [-1, 1]^2$ and the extraction operator are obtained.

Through the thickness integration is done by using the connectivity array (or IEN array). Using this array we determine which functions have a support in a given element. Assume that we use a quadratic B-spline defined over a knot vector of $\mathcal{T} = [0, 0, 0, \frac{1}{2}, 1, 1, 1]$, see also Figure 6. This definition leads to two elements of $[0, \frac{1}{2}]$ and $[\frac{1}{2}, 1]$ over the thickness and four global basis functions. Each element support $p_h + 1 = 3$ basis of the global basis. The IEN array is:

$$[\mathbf{IEN}]_{ne \times p_h+1} = \begin{pmatrix} 1 & 2 & 3 \\ 2 & 3 & 4 \end{pmatrix}_{2 \times 3} \tag{55}$$

The assembly of the element stiffness matrices can also be done according to the shared basis functions (number 2 and 3 in this case). It starts from the strain-displacement matrix $\mathbf{B}$:

$$[\mathbf{B}] = \left[\mathbf{B}_{e_1}^1, \ \mathbf{B}_{e_1}^2 + \mathbf{B}_{e_2}^2, \ \mathbf{B}_{e_1}^3 + \mathbf{B}_{e_2}^3, \ \mathbf{B}_{e_2}^4\right] \tag{56}$$

which is subsequently used in the calculation of the material part of the stiffness matrix $\mathbf{K}^{\text{mat}}$ in equation (47). The same steps are followed for the matrix $\mathbf{\Lambda}$ in equation (50) for the calculation of the geometrical part of the stiffness matrix $\mathbf{K}^{\text{geom}}$.

4.2. Modelling weak and strong discontinuities in the displacement field

As has been mentioned in Section 3.1, B-spline and NURBS basis functions are C^{p-k} continuous at a knot with multiplicity k. This means that we are able to control the continuity of the basis functions at a knot by arbitrarily selecting the multiplicity. This property is useful in modelling traction-free cracks and adhesive interfaces (strong discontinuity) and layered structures with C^0 continuity between the layers (weak discontinuity) [13].

Figure 8 shows the steps in order to make a discontinuity in the thickness direction of a shell structure. Assume that a quadratic B-spline basis function H_i defined over a knot vector $\mathcal{T} = [0, 0, 0, \frac{1}{2}, 1, 1, 1]$ has been used in the thickness of the shell. This gives us four basis functions which are all C^1 continuous at $\zeta = \frac{1}{2}$. Now suppose that we want to have a composite shell consisting of two layers of equal thickness. The deformation of composite structures requires a unique displacement at the interfaces and different strain fields in the adjacent layers. In the example of Figure 8 this is simply achieved by having a displacement field which is C^0 continuous at the interface $\zeta = \frac{1}{2}$. This leads to the new knot vector $\mathcal{T} = [0, 0, 0, \frac{1}{2}, \frac{1}{2}, 1, 1, 1]$. Henceforth, we will denote this element as the layered CSIGA element. Subsequently, the complete separation of the layers is obtained if we insert the second knot as: $\mathcal{T} = [0, 0, 0, \frac{1}{2}, \frac{1}{2}, \frac{1}{2}, 1, 1, 1]$, and this element will be denoted as the discontinuous CSIGA element. Figure 8 shows the corresponding basis functions through the knot insertion process.

It is important to note that if this method to introduce weak or strong discontinuities is adopted in the construction of a single volumetric B-spline or NURBS patch, the inserted discontinuity will have a global influence, i.e. it will propagate throughout the patch. While this is not a problem for when weak discontinuities are inserted to model layers, it can be restrictive when used to model delamination by means of strong discontinuities. In Section 5.6 we will demonstrate how linear constraints can be used to localize strong discontinuities in order to realistically mimic delaminations. In a further study we will develop a versatile method to localize strong discontintuities. This can potentially be achieved by adopting a localized definition of the basis functions – as is essentially done in T-splines – and has already been demonstrated in the context of cohesive-zone modelling [13].

5. Numerical simulations

The isogeometric continuum shell formulation is now verified and assessed through different examples. We refer to the proposed class of shell elements as CSIGA, see Table 1. In this table we distinguish between three cases for the continuum shell element: (i) without C^0 planes between the layers (lumped), (ii) with C^0 planes between the layers (layered), and (iii) with C^{-1} planes to simulate static delamination (discontinuous). Different orders of interpolation can be used in the plane
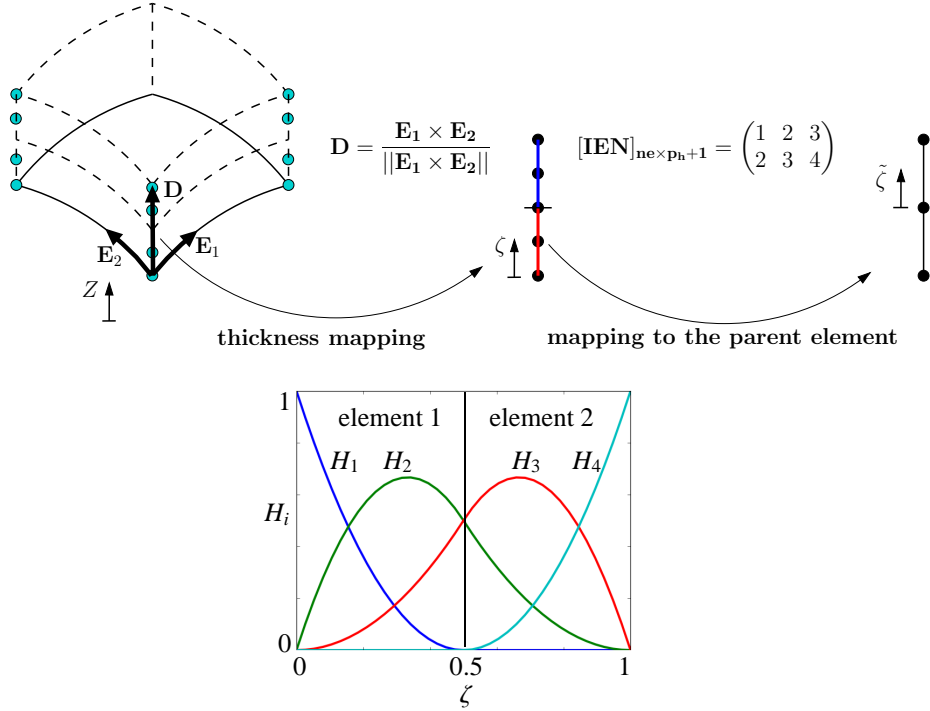
Figure 6: A quadratic B-spline basis function to be used for through the thickness discretization in the deformed configuration. The basis functions are defined over a knot vector of $[0, 0, 0, \frac{1}{2}, 1, 1, 1]$ which gives two elements over $[0, \frac{1}{2}]$ and $[\frac{1}{2}, 1]$. The numerical integration is done by defining the IEN-array which determines which functions have support in a given element. It should be noted that we do not consider any control point in the thickness direction where the thickness director $\mathbf{D}$ can be calculated directly from the in-surface base vectors $\mathbf{E}_1$ and $\mathbf{E}_2$.

as well as in the out-of-plane direction for each case. For instance, in the remainder "lumped(3,2)" will denote a CSIGA element without C^0 (weak discontinuity) planes between the layers, with a third-order NURBS/T-spline interpolation in the plane, and a second-order B-spline in the thickness direction.

In the beginning we examine the locking problem which is typical for shell elements. We proceed the simulations by a linear calculation on a composite panel, which aims to capture the global and local behavior of the panel (deflection and stress distribution, respectively). Then, the element will be tested using some geometrically non-linear examples of a pinched hemisphere and pinched cylinder with inward and outward loads. These simulations are followed by modelling buckling of delaminated zones in layered panels.

5.1. Locking

In this section we investigate shear locking and membrane locking which can occur when decreasing the thickness of shell elements. A clamped plate and a cylindrical shell, both under bending loads are used to assess the locking phenomenon.

5.1.1. Shear locking

Figure 9 shows the geometry of a plate subject to bending [11]. The plate has a Young's modulus $E = 1.0^8$ Pa and a Poisson's ratio $\nu = 0.3$. The dimensions of the plate are: $L = 10$ m, $b = 1$ m and the thickness t varies through the test. The plate is clamped at one end and a transverse load $q_z = 100t^3$ is applied at the other end.

As a reference value we consider the displacement at the free end according to the beam theory, $\delta = PL^3/3EI$ which results in $\delta = 0.004$ m for this test. The numerical simulation is done with two meshes of 64 CSIGA lumped(2,2) and 64 CSIGA lumped(3,2) elements. Figure 10 shows the obtained normalized displacements for different ratios of L/t. It is clear that employing second order and third order NURBS basis functions for the in-plane discretization result in shear locking free behaviour as the thickness of the plate reduces.

5.1.2. Membrane locking

Membrane locking can occur in curved structures [8, 9]. Therefore, a cylindrical shell as shown in Figure 11 is modelled. The shell has a radius of $R = 10$ m and a width of $b = 1$ m. Young's modulus and Poission's ratio are 1000 Pa and $\nu = 0$ respectively. The cylindrical shell is clamped at one edge and subjected to a constant distributed load of $q_x = 0.1t^3$. An analytical solution based on the Bernoulli beam theory gives a value of approximately 0.942 for the radial displacement.

The numerical results for various meshes and thicknesses are presented in Figure 12. In the figure, the mesh size shows the number of elements in the radial direction, while only one element has been used in the width direction. According to the results, a low number of elements of order two, 16 CSIGA lumped(2,2) elements, exhibit membrane locking. Keeping the NURBS order fixed and increasing the number of elements to 64 removes locking. Employing 16 third-order NURBS elements the results are locking-free as well.

8
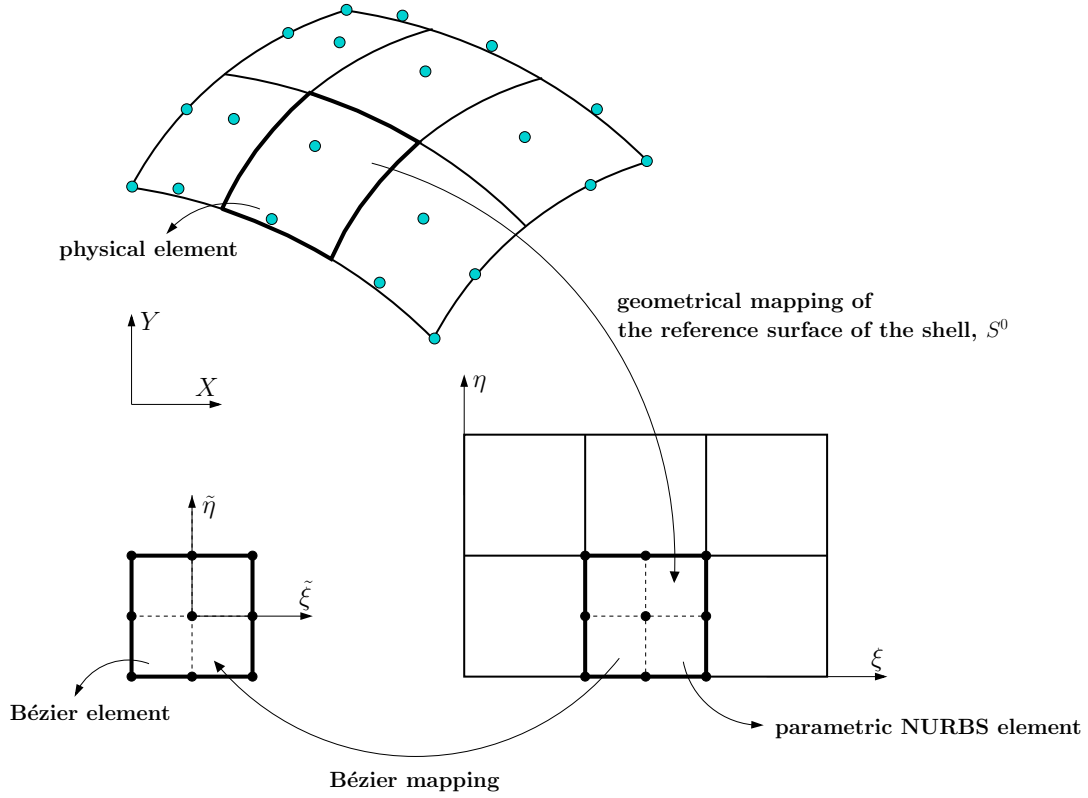
Figure 7: Numerical integration on the reference surface of the shell is done using the extraction operator. The geometry of the reference surface is mapped to the corresponding NURBS parametric space. A second mapping is made onto the Bézier space where the extraction operator and the parent element are obtained.
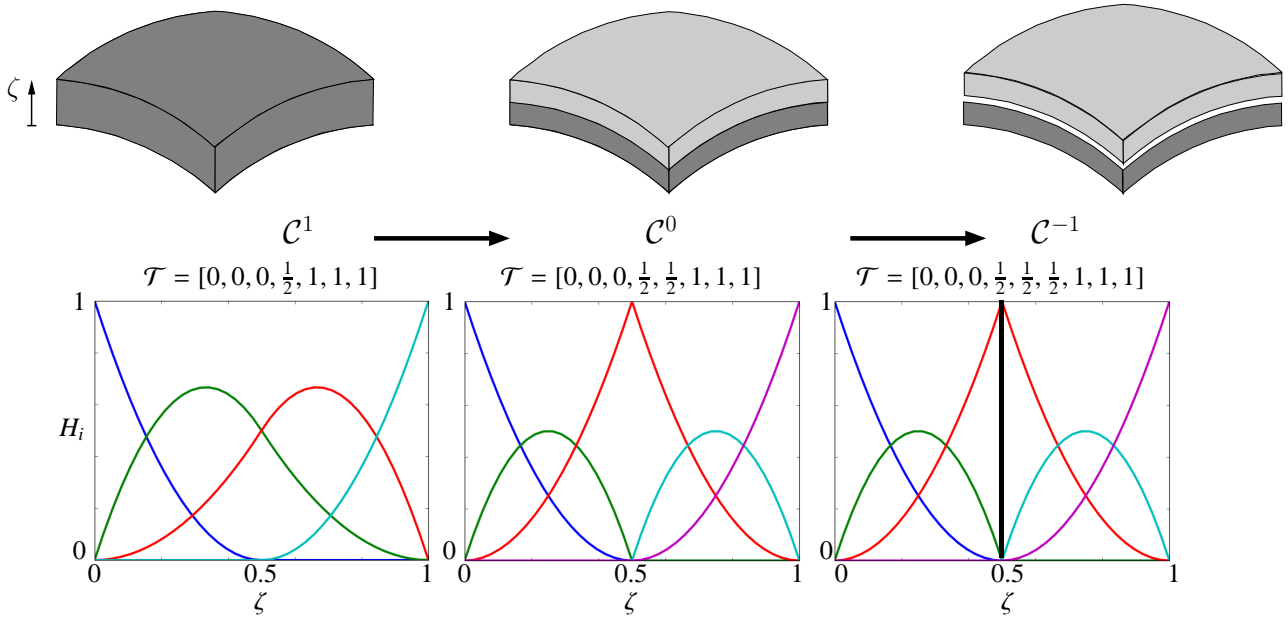
Figure 8: Schematic representation of introducing a discontinuity in the thickness direction of a shell. Weak and strong discontinuities between the layers of a composite shell are created by knot insertion.

5.2. Composite laminate

The performance of the shell element is studied in the simulation of the deflection of a multi-layer composite panel. In conventional shell models, these structures are often simulated with a single element in the thickness direction. This is generally sufficient for calculating displacements, but it does not

Table 1: Nomenclature of solid-like and continuum shell elements.

Model	In-plane discretization	Out-of-plane discretization
SLS [10]	1st or 2nd order Lagrange	1st order Lagrange
SLSBEZ(p) [12]	p^{th} order NURBS / T-Spline	1st order Lagrange
CSIGA(p, q)		
lumped	p^{th} order NURBS / T-Spline	q^{th} order B-Spline
layered	p^{th} order NURBS / T-Spline	q^{th} order B-Spline with C^0 continuities at each interface
discontinuous	p^{th} order NURBS / T-Spline	q^{th} order B-Spline with one C^{-1} continuity to represent a delamination. The other interfaces are C^0 continuous.
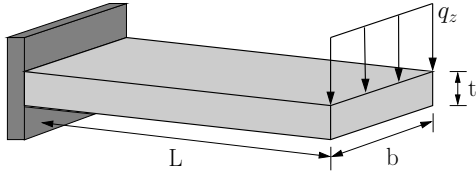
Figure 9: Geometry of the clamped plate under bending.
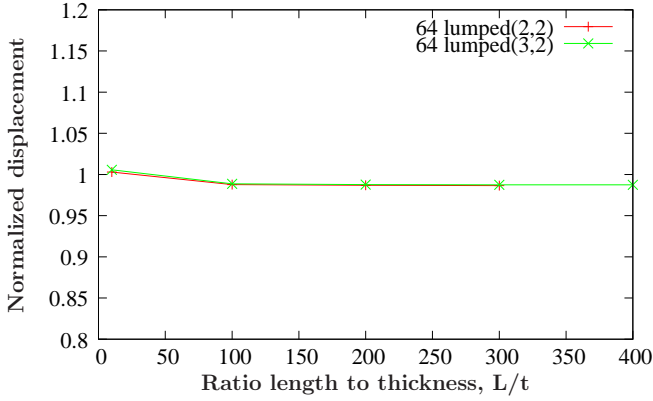
Figure 10: Normalized displacement of the plate under bending obtained for different ratios of L/t.
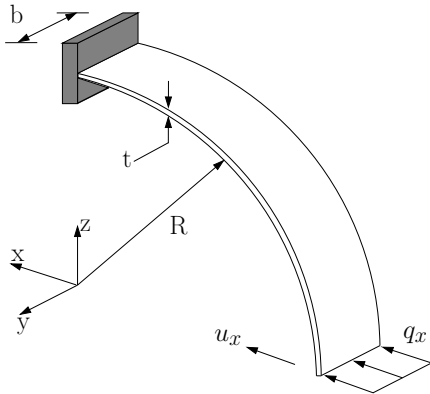
Figure 11: Geometry of the cylindrical shell

Figure 12: Cylindrical shell, displacement u_x for different ratios of R/t.
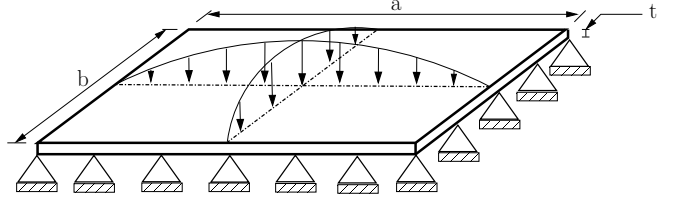
Figure 13: Geometry, boundary conditions and loading of a rectangular panel.

layers of a unidirectional material, with a stacking sequence $[0, 90, 0]_s$. Each layer is 0.2 mm thick, so that the total thickness of the shell is 1.2 mm. The layers can be modelled as a transversely isotropic material with $E_1 = 130$ GPa, $E_2 = E_3 = 7$ GPa, $\nu_{12} = 0.33$ and $G_{12} = 5$ GPa. The panel is simply supported on all four sides and is loaded by a distributed load

$$q_z = q_0 \sin \frac{\pi x}{a} \sin \frac{\pi y}{b}$$

with $q_0 = 1$ MPa.

The panel has been simulated for three different discretizations: second-order in the thickness direction, fourth-order in the thickness direction, and second-order per layer with weak discontinuities at the boundaries between the layers.

The analytical solution can be obtained from classical laminate theory. The deflection of the mid point of the panel is equal to -2.62×10^{-5} m. Figure 14 shows σ_{xx} in the mid-point of the panel as a function of the thickness coordinate

allow for computing the stresses and strains in the individual layers accurately.

We consider the square laminate shown in Figure 13. The panel has dimensions $a \times b = 0.6 \times 0.4$ m and consists of six

10

of the shell obtained for different discretizations. The results from one second-order and one fourth-order B-spline element, lumped(3,2) and lumped(3,4), respectively, lead to the same stress distribution as that of a second-order B-spline per layer (weak discontinuities at layer boundaries). All the results are in agreement with the analytical solution from the classical laminated plate theory. Moreover, the deflection at the mid-point of the panel is in agreement with the analytical solution.
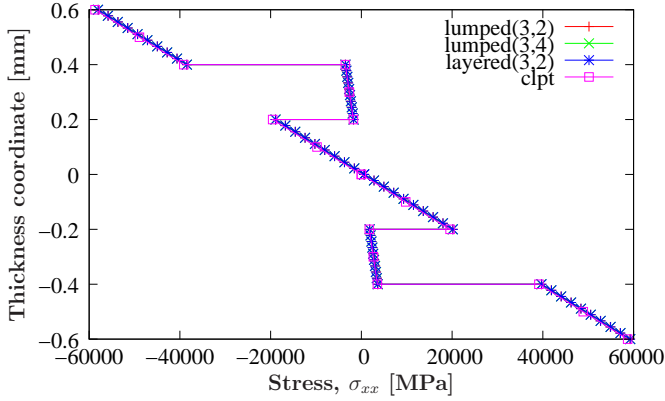
Figure 14: σ_{xx} at the mid-point as a function of the thickness of the panel. The thickness of the plate is 1.2 mm.

Next, the ability of the shell element to compute interlaminar stresses is examined. This issue is of importance when damage and failure of composite materials need to be considered in the simulations. The normal stress σ_{zz} is presented in Figure 15 as a function of thickness of the shell. By using third-order and second-order B-splines per layer, layered(3,3) and layered(3,2) elements, respectively, which are C^0 continuous at the interfaces, we can capture a σ_{zz} distribution in the thickness direction, which is zero through most of the thickness and equals $q_0 = 1$ MPa at the top surface. Adopting just one element of second-order and of fourth-order B-splines, lumped(3,2) and lumped(3,4), respectively, for the discretization in the thickness direction results in a fluctuation of the σ_{zz} distribution. From the results it is concluded that in order to compute σ_{zz} accurately we need to enforce C^0-continuity of the basis functions at the interfaces.

The simulations are now repeated for a ten times thicker panel with $q_0 = 100$ MPa. The results presented in Figure 16 show again that applying basis functions with C^0 continuity between the layers results stress distribution that can be expected for a thick panel. The jump at $z = 0$ is caused by the fact that the displacement boundary condition $u_z = 0$ at the edges has been enforced at $z = 0$.

5.3. Pinched hemispherical shell with a hole

A pinched hemisphere with a hole at the top has been used extensively as a benchmark problem for shell analysis to test the ability to describe nearly inextensional bending modes [22, 23, 24]. The geometric parameters and material properties employed in this test are summarized in Table 2. The
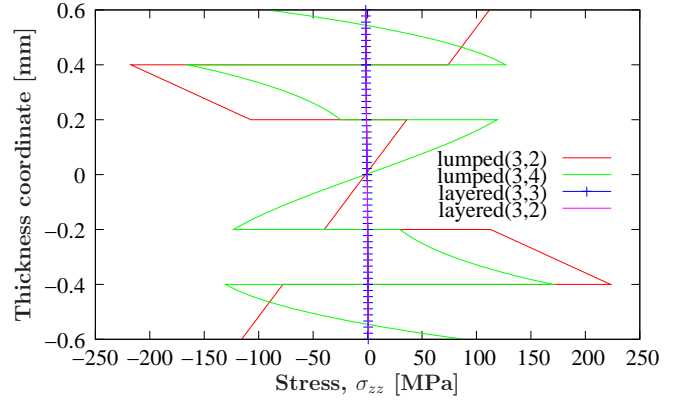
Figure 15: σ_{zz} at the mid-point as a function of the thickness of the panel. The thickness of the panel is 1.2 mm (thin panel).
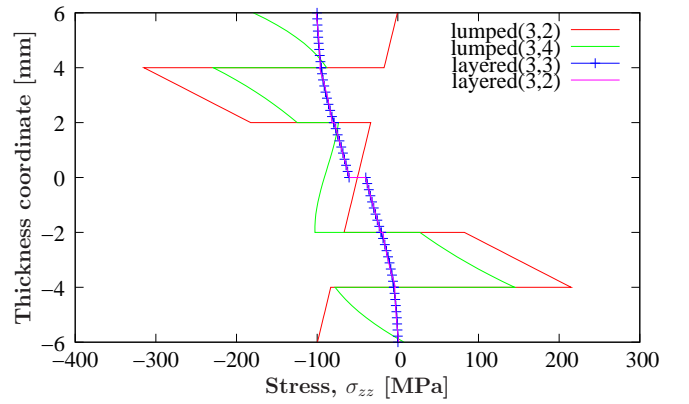
Figure 16: σ_{zz} at the mid-point as a function of the thickness of the panel. The thickness of the panel is 12 mm (thick panel).

shell is subjected to two opposite point loads. The bottom circumferential edge of the hemisphere is free. Due to the symmetry only a quarter of the shell needs to be modelled. The symmetric boundary conditions are applied by constraining the displacement degrees of freedom in the normal direction of the symmetry plane. The mesh and the applied boundary conditions are shown in Figure 17. ABAQUS has been used to generate a standard finite element solution, using a 16×16 mesh consisting of so-called S4R shell elements, which we will here use as a reference solution.

Table 2: Geometric parameters and material properties for the pinched hemisphere.

Radius R	Thickness t	Young's modulus E	Poisson's ratio ν
10.0 m	0.04 m	6.825×10^7 Pa	0.3

Figure 18 shows the load-displacement curves of the pinched hemisphere that have been obtained for different meshes. A mesh of 16×16 CSIGA elements of type lumped(3,2) leads to results that are close to the traditional finite element solution (using S4R elements). The graph also shows the result from a 16×16 mesh of SLSBEZ elements, which is slightly stiffer than
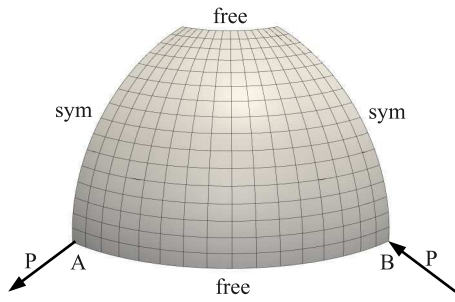
Figure 17: The mesh for a quarter model and the boundary conditions.

those obtained with the CSIGA and S4R elements.
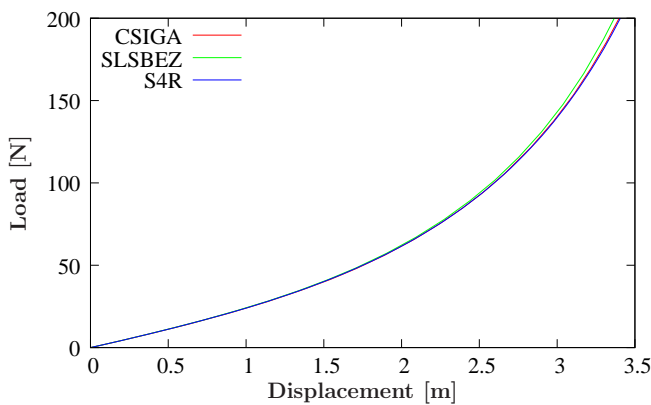
Figure 18: The load P as a function of the displacement at point A for the pinched hemisphere.

5.4. Pinched cylinder with free ends

The pinched cylinder with free ends shown in Figure 19 is used next to assess the element performance. The cylinder has a length L = 10.35 m, a radius R = 4.935 m, a thickness t = 0.094 m, a Young's modulus E = 10500 MPa and a Poisson's ratio v = 0.3125. The cylinder has free edges at the ends, and it is loaded by two centrally located diametrically opposed point forces, which pull in the outward direction. Due to symmetry considerations only one-eight of the cylinder needs to be modelled.

The initial response is dominated by the bending stiffness which induces large displacements at relatively low load levels. This changes into a very stiff response when the displacement become larger. Finite rotations occur afterwards, thus making the pinched cylinder with free ends a challenging test for element performance [25, 26, 27].

Figure 20 shows the load-displacement curves of this example. The results have been obtained with a mesh of 16×16 CSIGA elements of type lumped(3,2), a mesh of 16×16 SLS-BEZ elements and a mesh of 16×8 of S4R elements imple-
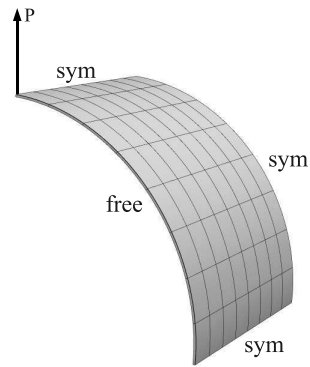
Figure 19: Pinched cylinder with free ends

mented in ABAQUS. The magnitude of the load is that for the complete cylinder and the displacement is measured at the point where load is applied. From Figure 20 it can be seen that the results from different elements are very close, however the CSIGA elements show a softer response.
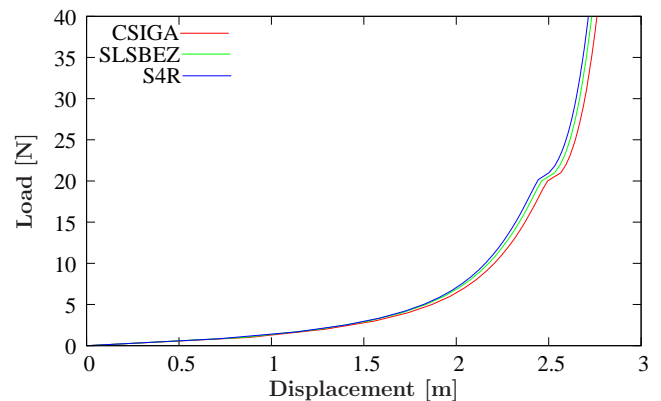
Figure 20: Load-Displacement diagram of pinched cylinder with free ends.

5.5. Pinched cylinder with rigid diaphragm

The problem of a pinched cylinder with a rigid diaphragm at the ends has been studied by several authors [28, 29, 30] in order to test the convergence behaviour and non-linear performance of shell elements. Since large rotations occur the problem provides a test for the finite rotation capability of the shell formulation. The cylinder has a length L = 200 mm, a radius R = 100 mm, a thickness t = 1 mm, a Young's modulus E = 30000 N/mm^2 and a Poisson's ratio v = 0.3. The cylinder is loaded by two centrally located, diametrically opposed point forces P, which push inwards. Using symmetry only one-eighth of the structure needs to be modelled.

Numerical simulation have been performed using CSIGA, SLSBEZ and S4R elements. Because of the need for mesh refinement at the free edge T-spline functions have been used for the in-plane discretization for both the CSIGA and SLSBEZ el-

ements, see Figure 21. The use of T-splines at the left free edge has been discussed in Ref. [12].
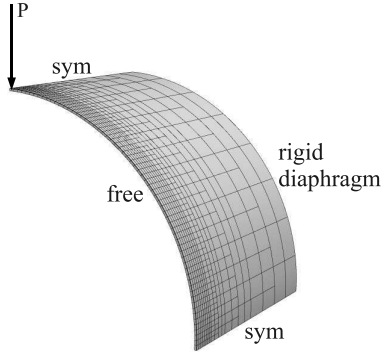
Figure 21: Pinched cylinder with rigid diaphragm

The results of the simulations are shown in Figure 22. The magnitude of the load is that for the complete cylinder and the displacement is measured at the point where load is applied. The CSIGA elements integrated with a $4 \times 4 \times 2$ integration scheme show locking for displacement level higher than 30 mm. Repeating the simulation with a $2 \times 2 \times 2$ integration scheme improves the results and compares well with those of the SLSBEZ and S4R elements.
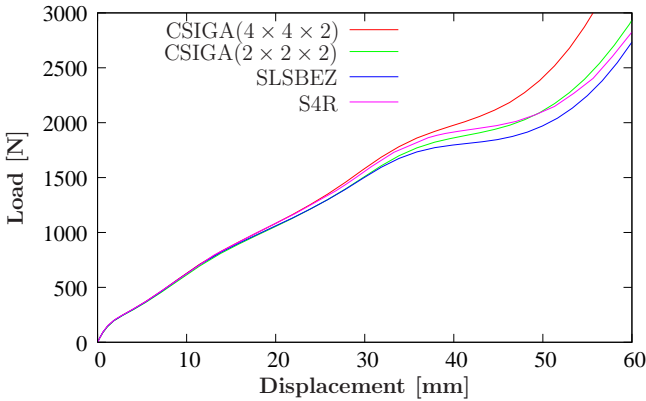
Figure 22: Load-Displacement diagram of pinched cylinder with rigid diaphragm.

5.6. Buckling of static delaminations

In the final examples, we will study the possibility to insert a delamination in layered structures by means of introducing a strong discontinuity through the thickness. The panels tested in the examples are partially delaminated over a strip and over a circular region, respectively.

5.6.1. Buckling of plate with initial strip delamination

We consider the panel shown in Figure 23. The panel has unit dimensions and consists of two layers of an isotropic material. The material properties are: $E = 2 \times 10^4$ MPa and $\nu = 0.3$. The top layer has a thickness 0.01 m and the bottom layer 0.09 m.

The top layer is partially delaminated over a width of 0.75 m. This delamination is modelled by a strong discontinuity in the thickness direction.
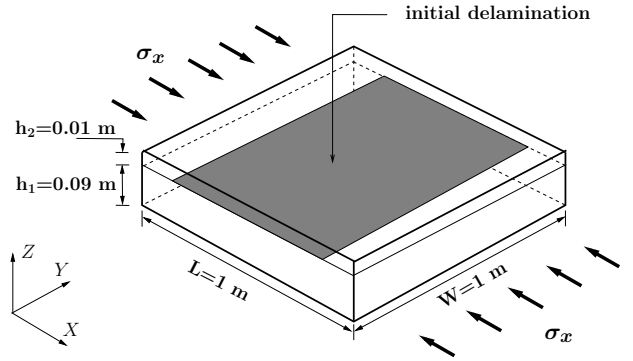
Figure 23: Geometry of the panel with a strip initial delamination, which is located between the two layers.

We start by defining the through-the-thickness B-spline functions over a knot vector of $\mathcal{T} = [0, 0, 0, 0.9, 0.9, 0.9, 1, 1, 1]$. This gives two layers in the thickness which are fully delaminated. The area that is not delaminated can be modelled by applying a linear constraint between the lower layer and the upper layer. Figure 24 shows the third-order NURBS meshes used for this example. In these meshes the control points are shown in red and blue. Using equation (37) the vector of degrees of freedom $\mathbf{\Phi}_i$ for each control point is written as:

$$\mathbf{\Phi}_i = [a_x^1, a_y^1, a_z^1, ..., a_x^6, a_y^6, a_z^6]^T \quad , \quad i = 1, 2, ..., n \quad (57)$$

The linear constraint is now applied to the red control points as:

$$a_x^3 = a_x^4 \ , \ a_y^3 = a_y^4 \ , \ a_z^3 = a_z^4 \quad (58)$$

By doing so the degrees of freedom with the superscript 3 and 4 have the same values at the interface of the two layers. It should be noted that the linear constraint is not applied to the blue control points. Referring to the basis functions shown in Figure 24, it can be seen that the basis functions corresponding to the blue control points have a support over the whole delaminated area in the parametric space. Therefore, by excluding their corresponding degrees of freedom from the linear constraint space the delaminated area can be preserved.

An issue in delamination modelling is the proper selection of the order of the continuity of the NURBS basis functions at the delamination fronts. Figure 25 shows the results obtained with the third-order NURBS basis which are C^2 continuous at the delamination fronts. The figure presents the out-of-plane displacement versus the axial stress σ_{xx} for different mesh sizes. An analytical solution for the buckling stress of a clamped panel with thickness of $h = 0.01$m and length $l = 0.75$m was formulated by Kachanov [31]:

$$\sigma_{cr} = \frac{\pi^2 E}{3(1 - \nu^2)} \left(\frac{h}{l}\right)^2 = 12.84 \, \text{MPa} \quad (59)$$

A very fine mesh of 192 elements is used as the reference solution. As can be seen, the results obtained by 16, 32 and 64 element converge to the reference and the analytical solutions.

13
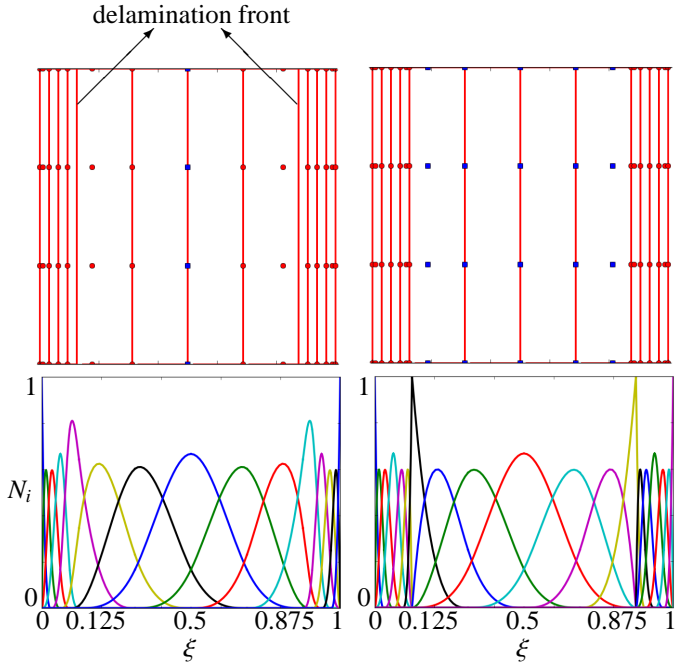
Figure 24: Third-order NURBS meshes used for the panel with initial strip delamination. The left mesh uses C^2 continuous basis at the delamination front while in the right mesh C^0 continuous basis functions are used at the delamination front.
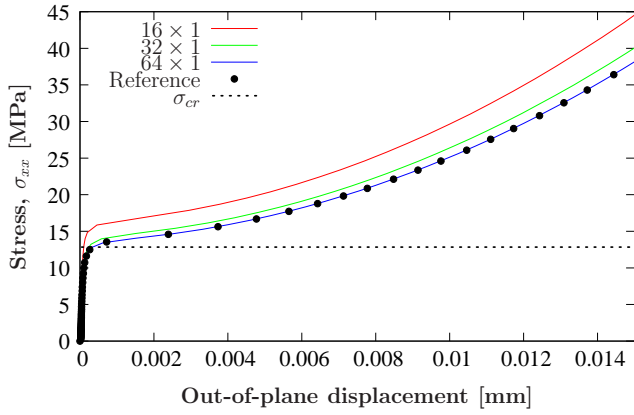
Figure 25: Diagram of the axial stress σ_{xx} vs the out-of-plane displacement of the plate with an initial strip delamination. The used meshes are C^2 at the delamination fronts.

We repeat the simulation using third-order NURBS basis function, but with a C^0 continuity at the delamination fronts, in order to exactly capture the Dirichlet boundary condition at this position. Figure 26 shows that using 48 NURBS elements the obtained critical stress is in agreement with the reference solution of 192 elements and the analytical solution. Accordingly, by applying C^0 continuous basis functions at the delamination front we can properly capture the boundary condition, which is a basic assumption in the analytical expression for the buckling load. Figure 27 shows a schematic representation of the delamination opening resulting from meshes with and without C^0 con-
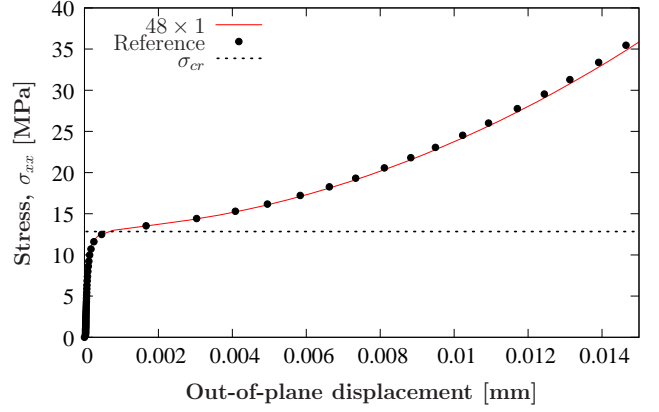
Figure 26: Diagram of the axial stress σ_{xx} vs the out-of-plane displacement of the plate with an initial strip delamination. The used meshes are C^0 at the delamination fronts.

tinuity at the delamination fronts. As it can be seen, for the C^0 case the effective length of the initial delamination l_e is larger than that resulting from the C^2 mesh. Referring to the analytical solution for the critical buckling stress i.e. equation (59), it is clear that the buckling load is proportional to the inverse of the initial delamination length l. Therefore, for an equal number of elements, a C^0 mesh at the delamination front will result in a smaller critical buckling stress, which explains the difference between the obtained results. However, the additional effort of enforcing C^0 continuity probably does not outweigh the computational gain, since with 64 C^2 continuous elements the same result was obtained. This holds a fortiori when propagating delamination fronts are considered.
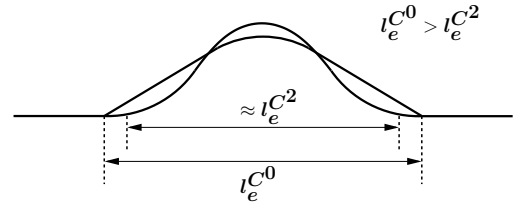
Figure 27: Schematic representation of the delamination opening obtained with meshes which are C^2 and C^0 continuous at the delamination front.

5.6.2. Glare panel with a circular delamination

In this section the buckling behavior of a Glare panel with initial circular delamination under uniaxial compressive load is examined. The specimen geometry is shown in Figure 28. The panel consists of an aluminium layer with thickness $h_1 = 0.2$ mm and a Glare 0/90° prepreg layer with a thickness 0.3 mm. A circular delamination with radius 8 mm is assumed between the layers. In order to avoid global buckling, a thick layer of aluminum is attached to the panel. Table 3 contains the material parameters of the Glare prepreg.

An advantage of using NURBS basis functions is that we are able to model an exact circular delamination shape.

14
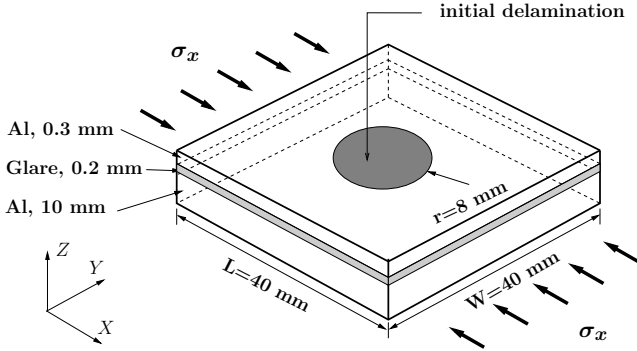
Figure 28: Geometry of the Glare panel with a circular initial delamination, which is located between the top aluminum layer and the Glare layer.

Table 3: Material parameters for 0/90° Glare prepreg.

$E_{11} = 33170$ MPa	$E_{22} = 33170$ MPa	$E_{33} = 9400$ MPa
$G_{12} = 5500$ MPa	$G_{23} = 5500$ MPa	$G_{13} = 5500$ MPa
$\nu_{12} = 0.195$	$\nu_{23} = 0.032$	$\nu_{13} = 0.032$

Similar to the previous example the delamination is modelled by a strong discontinuity between the layers where a linear constraint will preserve the adhesion at the remainder of the panel. In this case we define through the thickness B-spline basis functions over a knot vector of $\mathcal{T} = [0, 0, 0, 0.952, 0.952, 0.971, 0.971, 0.971, 1, 1, 1]$. Accordingly the linear constraint is written as:

$$a_x^5 = a_x^6 \ , \ a_y^5 = a_y^6 \ , \ a_z^5 = a_z^6 \tag{60}$$

Because of the symmetry only one quarter of the geometry is analyzed. Figure 29 shows a second-order NURBS mesh for this example. The basis functions have been chosen to be C^0 continuous at the delamination front. Figure 30 presents the out-of-plane displacement *vs* the axial stress σ_{xx} for two fine NURBS meshes. Both meshes lead to the same result.

6. Concluding remarks

A continuum shell element has been formulated that is based on the isogeometric concept. NURBS basis functions have been used to parametrize the reference surface, and a B-spline shape function has been employed in the thickness direction. In this manner, a complete three-dimensional representation of the shell is obtained. The shell formulation combines the advantages of a full, three-dimensional stress and strain representation that allows for the straightforward implementation of constitutive relations such as plasticity or damage, with the advantages of isogeometric analysis, including the exact description of the geometry, the use of the design-through-analysis concept, and the accurate prediction of stress fields. The latter property is also important for the prediction of the onset of plasticity, damage, or delaminations due to high transverse stresses.

In this paper, the performance of the isogeometric continuum shell element has been assessed by means of a number of linear
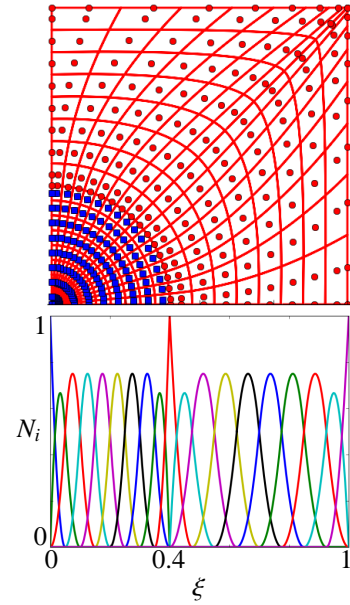
Figure 29: The second-order NURBS mesh used for the panel with circular delamination. The basis function are C^0 continuous at delamination front.
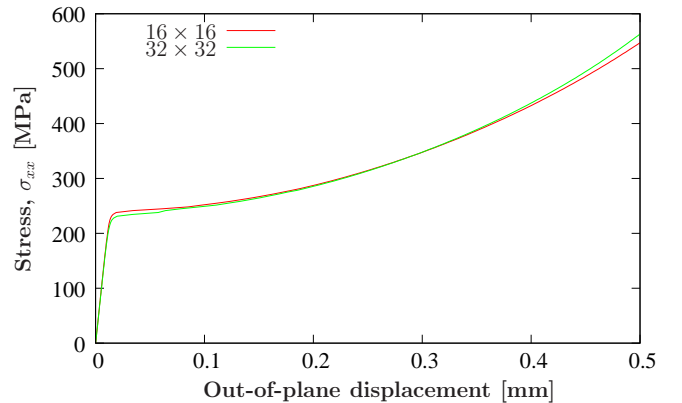
Figure 30: Diagram of the axial stress σ_{xx} *vs* the out-of-plane displacement of the plate with an initial circular delamination.

and non-linear examples. First, the performance with respect to shear and membrane locking was examined for a straight and for a curved clamped strip. The element was found locking-free at least for length to thickness ratios up to 400 provided that cubic splines were used for the in-plane discretization or quadratic splines with a sufficiently fine discretization. Next, a unidirectional composite panel consisting of six layers of $[0, 90, 0]_s$ has been tested under a sinusoidal distributed pressure load. It was shown that the global behavior of the panel, deflection and the in-plane stress distribution, can be well captured by using just one element of B-spline basis function in the thickness direction. Furthermore, the intralaminar stress distribution requires the through the thickness parametrization to be C^0 continuous at interfaces. This property was achieved by employing knot insertion in the thickness direction. Doing so, the transverse normal stress σ_{zz} as a function of the thickness of the panel was

obtained.

As benchmark tests for geometrically non-linear performance, a pinched hemisphere with a hole and a pinched cylinder with free ends and with a rigid diaphragm were used. The results are in agreement with reference solutions by the ABAQUS S4R shell element, provided that in the last example a sufficiently low order integration was used in the plane.

An important feature of the proposed element is its ability to model static delamination buckling in composite materials. Delamination is modelled as a strong discontinuity between the layers by means of knot insertion in the through the thickness parametrization. To model bonding in a partially delaminated area, linear constraints were locally applied to the upper and lower layers.

A panel with an initial strip delamination under axial compressive load was studied. By employing C^0 continuous basis functions at the delamination fronts it is possible to capture the Dirichlet boundary condition at these fronts. The analytical buckling load was reproduced accurately.

As a final example, the buckling behavior of a composite panel with initial circular delamination was studied, where it is noted that the NURBS mesh results in an exact parametrization of the circular shape of the delaminated area. The panel was subjected to an axial compressive load. By using a NURBS mesh with C^0 continuity at the delamination front the buckling load was computed accurately.

Acknowledgements

Appendix A. Derivation of virtual strain terms

Using equation (18) the virtual strain $\delta\gamma_{11}$, as an example, is written as:

$$\delta\gamma_{11} = \mathbf{g}_1 \cdot \delta\mathbf{u}_{,1} \tag{A.1}$$

using equation (6) for $\mathbf{g}_1$ where

$$\mathbf{g}_1 = \mathbf{G}_1 + \mathbf{u}_{,1} \tag{A.2}$$

is calculated as a total value at the beginning of each step. $\mathbf{G}_1$ is calculated at each integration point using equation (54) and $\mathbf{u}_{,1}$ is obtained using equation (38) as:

$$\mathbf{u}_{,1} = \sum_{j=1}^{m}\sum_{i=1}^{n} S_{i,\xi}(\xi,\eta)H_j(\zeta)\left(a_x^{ji}\cdot\mathbf{i}_x + a_y^{ji}\cdot\mathbf{i}_y + a_z^{ji}\cdot\mathbf{i}_z\right) \tag{A.3}$$

Similarly, the virtual strain term is given as:

$$\delta\mathbf{u}_{,1} = \sum_{j=1}^{m}\sum_{i=1}^{n} S_{i,\xi}(\xi,\eta)H_j(\zeta)\left(\delta a_x^{ji}\cdot\mathbf{i}_x + \delta a_y^{ji}\cdot\mathbf{i}_y + \delta a_z^{ji}\cdot\mathbf{i}_z\right) \tag{A.4}$$

Appendix B. The local strain–displacement matrix, $\mathbf{B}_L$

The virtual strains and the corresponding $\mathbf{B}$ matrix in equation (40) are stated in the non-orthonormal curvilinear basis vectors which should be transformed to the element local frame according to equation (15). The transformed $\mathbf{B}$ matrix is represented by $\mathbf{B}_L$. Using the notation that:

$$\ell_{ij}^{kl} = t_{ki}t_{lj} \tag{B.1}$$

the column N of the matrix which relates the virtual strains to the virtual displacement in the local frame of reference is given by:

$$\mathbf{B}_L = \begin{bmatrix} b_{1N}\ell_{11}^{11} + b_{2N}\ell_{11}^{22} + b_{3N}\ell_{11}^{33} + b_{4N}\frac{1}{2}(\ell_{11}^{12} + \ell_{11}^{21}) \\ +b_{5N}\frac{1}{2}(\ell_{11}^{23} + \ell_{11}^{32}) + b_{6N}\frac{1}{2}(\ell_{11}^{31} + \ell_{11}^{13}) \\[1em] b_{1N}\ell_{22}^{11} + b_{2N}\ell_{22}^{22} + b_{3N}\ell_{22}^{33} + b_{4N}\frac{1}{2}(\ell_{22}^{12} + \ell_{22}^{21}) \\ +b_{5N}\frac{1}{2}(\ell_{22}^{23} + \ell_{22}^{32}) + b_{6N}\frac{1}{2}(\ell_{22}^{31} + \ell_{22}^{13}) \\[1em] b_{1N}\ell_{33}^{11} + b_{2N}\ell_{33}^{22} + b_{3N}\ell_{33}^{33} + b_{4N}\frac{1}{2}(\ell_{33}^{12} + \ell_{33}^{21}) \\ +b_{5N}\frac{1}{2}(\ell_{33}^{23} + \ell_{33}^{32}) + b_{6N}\frac{1}{2}(\ell_{33}^{31} + \ell_{33}^{13}) \\[1em] b_{1N}(\ell_{12}^{11} + \ell_{21}^{11}) + b_{2N}(\ell_{12}^{22} + \ell_{21}^{22}) + b_{3N}(\ell_{12}^{33} + \ell_{21}^{33}) \\ b_{4N}\frac{1}{2}(\ell_{12}^{12} + \ell_{21}^{12} + \ell_{12}^{21} + \ell_{21}^{21}) + b_{5N}\frac{1}{2}(\ell_{12}^{23} + \ell_{21}^{23} + \ell_{12}^{32} + \ell_{21}^{32}) \\ +b_{6N}\frac{1}{2}(\ell_{12}^{31} + \ell_{21}^{31} + \ell_{12}^{13} + \ell_{21}^{13}) \\[1em] b_{1N}(\ell_{23}^{11} + \ell_{32}^{11}) + b_{2N}(\ell_{23}^{22} + \ell_{32}^{22}) + b_{3N}(\ell_{23}^{33} + \ell_{32}^{33}) \\ b_{4N}\frac{1}{2}(\ell_{23}^{12} + \ell_{32}^{12} + \ell_{23}^{21} + \ell_{32}^{21}) + b_{5N}\frac{1}{2}(\ell_{23}^{23} + \ell_{32}^{23} + \ell_{23}^{32} + \ell_{32}^{32}) \\ +b_{6N}\frac{1}{2}(\ell_{23}^{31} + \ell_{32}^{31} + \ell_{23}^{13} + \ell_{32}^{13}) \\[1em] b_{1N}(\ell_{13}^{11} + \ell_{31}^{11}) + b_{2N}(\ell_{13}^{22} + \ell_{31}^{22}) + b_{3N}(\ell_{13}^{33} + \ell_{31}^{33}) \\ b_{4N}\frac{1}{2}(\ell_{13}^{12} + \ell_{31}^{12} + \ell_{13}^{21} + \ell_{31}^{21}) + b_{5N}\frac{1}{2}(\ell_{13}^{23} + \ell_{31}^{23} + \ell_{13}^{32} + \ell_{31}^{32}) \\ +b_{6N}\frac{1}{2}(\ell_{13}^{31} + \ell_{31}^{31} + \ell_{13}^{13} + \ell_{31}^{13}) \end{bmatrix} \tag{B.2}$$

[1] Hughes T.J.R, Cottrell J, Bazilevs Y. Isogeometric analysis: CAD, finite element, NURBS, exact geometry and mesh refinement. *Computer Methods in Applied Mechanics and Engineering* 2005; **194**: 4135-4195.

[2] Cottrell J, Hughes T.J.R, Bazilevs Y. *Isogeometric Analysis: Toward Integration of CAD and FEA*. John Wiley & Sons, Chichester, 2009.

[3] Sederberg T.W, Zheng J, Bakenov A, Nasri A. T-splines and T-NURCCs. *ACM Transactions on Graphics* 2003; **22**:477-484.

[4] Kiendl J, Bletzinger K.U, Linhard J and Wüchner R. Isogeometric shell analysis with Kirchhoff-Love elements. *Computer Methods in Applied Mechanics and Engineering* 2009; **198**: 3902-3914.

[5] de Borst R, Crisfield M.A, Remmers J.J.C, Verhoosel C.V. *Non-linear Finite Element Analysis of Solids and Structures*. Wiley series in computational mechanics, Second edition, 2012.

[6] Benson D.J, Bazilevs Y, Hsu M.C and Hughes T.J.R. Isogeometric shell analysis: The Reissner-Mindlin shell. *Computer Methods in Applied Mechanics and Engineering* 2010; **199**: 276-289.

[7] Dornisch W, Klinkel S, Simeon B. Isogeometric Reissner-Mindlin shell analysis with exact calculated director vectors. *Computer Methods in Applied Mechanics and Engineering* 2012; http://dx.doi.org/10.1016/j.cma.2012.09.010.

[8] Bischoff M, Wall W, Bletzinger K.-U, Ramm E. Models and finite elements for thin-walled structures. In: *Encyclopedia of Computational Mechanics*, Eds. Stein E, de Borst R, Hughes T.J.R, Vol. 2, Chapter 3, pp. 59-137. Wiley: Chichester, 2004.

[9] Echter R, Oesterle B, Bischoff M. A hierarchic family of isogeometric shell finite elements. *Computer Methods in Applied Mechanics and Engineering* 2013; **254**: 170-180.

[10] Parisch H. A continuum-based shell theory for non-linear application. *International Journal for Numerical Methods in Engineering* 1995; **38**: 1855-1883.

[11] Hashagen F, de Borst R. Numerical assessment of delamination in fibre metal laminates. *Computer Methods in Applied Mechanics and Engineering* 2000; **185**: 141-59.

[12] Hosseini S, Remmers J.J.C, Verhoosel C.V, de Borst R. An isogeometric solid-like shell formulation for non-linear analysis. *International Journal for Numerical Methods in Engineering* 2013; **95**(3): 238–256.

[13] Verhoosel C.V., Scott M.A., de Borst R, Hughes T.J.R. An isogeometric approach to cohesive zone modeling. *International Journal for Numerical Methods in Engineering* 2011, **87**(1-5), 336–360.

[14] Reddy J.N. A simple higher-order theory for laminated composite plates. *Journal of Applied Mechanics* 1984; **51**: 745-752.

[15] Braun M, Bischoff M, Ramm E. Nonlinear shell formulations for complete three-dimensional constitutive laws including composites and laminates. *Computational Mechanics* 1994; **15**: 1-18.

[16] Remmers J.J.C, Wells G.N, de Borst R. A solid-like shell element allowing for arbitrary delaminations. *International Journal for Numerical Methods in Engineering* 2003; **58**: 2013-2040.

[17] Cox M.G. The numerical evaluation of B-splines. *IMA Journal of Applied Mathematics* 1972; **10**: 134-149.

[18] de Boor C. On calculating with B-splines. *Journal of Approximation Theory* 1972; **6**: 50-62.

[19] Borden M.J, Scott M.A, Evans J.A, Hughes T.J.R. Isogeometric finite element data structures based on Bézier extraction. *International Journal for Numerical Methods in Engineering* 2011; **87**: 15-47.

[20] Scott M.A, Borden M.J, Verhoosel C.V, Sederberg T.W, Hughes T.J.R. Isogeometric finite element data structures based on Bézier extraction of T-splines *International Journal for Numerical Methods in Engineering* 2011; **88**: 126-156.

[21] Piegl L, Tiller W. *The NURBS Book*, Second Edition. Springer-Verlag, New York, 1997.

[22] Betsch P, Gruttmann F, Stein E. A 4-node finite shell element for the implementation of general hyperelastic 3D-elasticity at finite strain. *Computer Methods in Applied Mechanics and Engineering* 1996; **130**: 57-79.

[23] Buechter N, Ramm E. Shell theory versus degeneration – a comparison in large rotation finite element analysis. *International Journal for Numerical Methods in Engineering* 1992; **34**: 39-59.

[24] Simo J.C, Fox D.D, Rifai M.S. On stress resultant geometrically exact shell model. Part III: computational aspects of nonlinear theory. *Computer Methods in Applied Mechanics and Engineering* 1990; **79**:21-70.

[25] Gruttman F, Stein E, Wriggers P. Theory and numerics of thin elastic shells with finite rotations. *Ingenieur-Archiv* 1989; **59**:54-67.

[26] Sansour C, Bednarczyk H. The Cosserat surface as a shell model, theory and finite-element formulation. *Computer Methods in Applied Mechanics and Engineering* 1995; **120**: 1-32.

[27] Sansour C, Bufler H. An exact finite element rotations shell theory, its mixed variational formulation, and its finite element formulation. *International Journal for Numerical Methods in Engineering* 1992; **34**: 73-115.

[28] Lindberg G.M, Olson M.D, Cowper G.R. New development in the finite element analysis of shells. *Quarterly Bulletin of the Division of Mechanical Engineering* 1969; **4**: 1-38.

[29] Bucalem M.L, Bathe K.J. Higher-order MITC general shell elements. *International Journal for Numerical Methods in Engineering* 1993; **36**: 3729-3754.

[30] Saleeb A.F, Chang T.Y, Graf W, Yingyeunyong S. A hybrid/mixed model for non-linear shell analysis and its application to large rotation problems. *International Journal for Numerical Methods in Engineering* **29**: 407-446.

[31] Kachanov L.M., 1998. Delamination buckling of composite materials. Dordrecht, The Netherlands, Kluwer academic publishers.